Practical Green's function approach to the simulation of elastic semi-infinite solids

Carlos Campañá and Martin H. Müser*
Department of Applied Mathematics, University of Western Ontario, London, Ontario, Canada N6A 5B7
(Received 17 May 2006; revised manuscript received 12 July 2006; published 21 August 2006)

This paper is concerned with the principles of Green's function-based molecular dynamics (GFMD) simulations of semi-infinite elastic solids and their application to various contact mechanical problems. A methodology to compute the (renormalized) elastic interactions of surface atoms is presented first. It is based on the fluctuation-dissipation theorem, with the help of which thermal fluctuations of atomic displacements can be related to the elastic Green's functions and thus to the effective coupling between surface atoms. We suggest a sparse representation of these renormalized spring constants and present numerical results for some simple two- and three-dimensional lattices. The renormalized elastic interactions can be obtained for relatively small systems and then be extrapolated to large systems. They incorporate the full elastic response of semi-infinite solids in a way that only surface atoms have to be considered in molecular dynamics simulations. The usefulness of GFMD is demonstrated by applying it to various idealized contact models, such as nonadhesive Hertzian contacts as well as nonadhesive contacts between flat, semi-infinite elastic solids and a self-affine, rigid substrate. In all cases, a zero probability density $P(p)$ for infinitesimally small contact pressures p is found, as predicted theoretically. If the self-affine, nonadhesive surfaces are under such high loads that the contact is complete, the pressure histogram can be represented by a Gaussian also in accordance with theoretical predictions. However, if the topography of the substrate resembles that of industrial steel surfaces and the loads are moderate, $P(p)$ decays exponentially for medium and large p in contradiction to theoretical predictions for randomly rough surfaces.

DOI: 10.1103/PhysRevB.74.075420 PACS number(s): 46.55.+d, 02.70.Ns, 68.35.Ja

I. INTRODUCTION

Many physical processes that are commonly associated with interfacial interactions can be strongly affected by long-range elastic deformation in the bulk. Examples are the epitaxial growth of metals on elastically deformable, crystalline substrates[1,2] and the contact mechanics or the friction between elastically deformable bodies with rough surfaces.[3–7] When modeling such interfaces by means of molecular dynamics (MD) or related atomistic simulation techniques, it may thus be necessary to include the effect of long-range elastic deformation of a system whose linear dimension normal to the interface is as large as the linear dimension $\mathcal{L}$ of the interface.[8] An all-atom simulation of these blocks will require significant computing time and memory. Without the implementation of multiscale techniques, the computational effort of a single time step algorithm would scale with $\mathcal{L}^3$, while using multiscale approaches can reduce the effort to scale approximately with $\mathcal{L}^2$. Thus, the speed-up of the computation can be tremendous if the value of $\mathcal{L}$ is in the order of 1000 times the typical size of an atom.

In the past, two different methodologies have been used to numerically analyze the elastic deformation of semi-infinite solids in atom-based simulations. In the first approach, the system is represented on ever more coarse-grained scales as one moves away from the zone of interest,[9–12] e.g., the interface. Calculations using this methodology to study the mechanical contact between three-dimensional systems have been presented recently.[4–6,8] The second type of approach is based on Green's function formulations for semi-infinite elastic lattices.[13–18] In a recent paper by Rudd and Broughton both types of approaches were combined within one framework:[19] Green's function-type techniques were used to connect the atomic region with the coarse-grained finite element description of the bulk material. This method allows for almost perfect transmission of elastic waves through the interface between the atomistic and the coarse-grained description. Despite these important advances, a Green's function-based simulation technique of semi-infinite solids has not yet been employed in practice, to the best of our knowledge. This comment concerns in particular the study of contact mechanics and the friction between two rough surfaces. Overcoming this shortcoming is the purpose of our work, which includes a description of how to efficiently obtain the elastic Green's functions for a given system. We do not intend to point out all the assets and drawbacks of each class of algorithm in detail. Instead, we will mainly content ourselves with a technical discussion of the Green's function approach. It shall only be said that the main advantage of GFMD is its fast rate of convergence while its main disadvantage is the lack of modeling plasticity.

The main idea behind GFMD is that all internal (harmonic) modes of an elastic body can be integrated out leading to effective interactions of those atoms whose degrees of freedom couple to an external force,[20] i.e., one calculates the renormalized interactions between the surface atoms. The idea does not only apply to static situations, but also extends to dynamics.[14,15,19–21] However, a (full) Green's function implementation for dynamics may not be suitable, because the dynamical coupling between different modes and the bookkeeping of memory functionals requires a large computational overhead. In this work, we will mainly be concerned with static properties.

Calculating elastic Green's function analytically is notoriously difficult even for relatively simple interactions and geometries such as simple square[16] or simple cubic[17] lattices with harmonic coupling between nearest and next-nearest

neighbors. This difficulty may well have been the main impediment for the use of Green's functions in the simulation of contact mechanics and friction between elastic bodies. The only Green's function-based numerical simulation of contact mechanics that we are aware of was done in the long-wavelength limit for one-dimensional interfaces.[22] However, for lattices other than simple Bravais lattices, such continuum approaches will need extensions along the lines that are presented here.

An important aspect of this paper is the suggestion to exploit the fluctuation-dissipation theorem to evaluate the elastic Green's function of homogeneous solids numerically, which facilitates their calculation. The main idea can be summarized as follows: A (small) solid block of the material of interest is observed under the influence of thermal noise. The correlation matrix (or Green's functions) of atomic displacements $\tilde{u}_\alpha(\mathbf{q})$ can be measured in reciprocal space, where α enumerates the Cartesian components and $\mathbf{q}$ is a wave vector lying within the interface. The inverse of the correlation matrix $\langle \tilde{u}^*_\alpha(\mathbf{q})\tilde{u}_\beta(\mathbf{q})\rangle$ (divided by the thermal energy) can be interpreted as the renormalized force constants in reciprocal space $\Phi_{\alpha\beta}(\mathbf{q})$. These force constants (or stiffness coefficients) can then be used in MD simulations. A similar scheme to obtain effective elastic interactions was used previously to ascertain the effective elastic coupling between self-assembled, ordered rodlike structures formed by block copolymers.[23]

It is also crucial for our approach that the results for the $\Phi_{\alpha\beta}(\mathbf{q})$'s can be easily extrapolated from small systems to large systems if they are represented as Fourier series or related sums. These sums are quickly converging provided that the generating functions are properly chosen. Another important aspect of GFMD is that displacements for different $\mathbf{q}$ vectors decouple, if the semi-infinite solid is translationally invariant. For a lattice with basis, similar comments apply, however, the indices α and β must be expanded to also include an index of the atom numbers in the basis. Last, due to the Green's functions being nonlocal in space, convergence to equilibrium is extremely fast.

As will be demonstrated in this paper, GFMD allows one to tackle questions evolving around the contact mechanics of solids quite efficiently. The first test case will be a Hertzian contact, for which we can ascertain how many grid points per contact radius need to be taken to reliably predict pressure histograms. We will also investigate the contact mechanics between self-affine surfaces and test predictions based on analytical theories[24,25] and finite-element calculations.[4–6]

The remainder of this paper is organized as follows: In Sec. II, we provide the theoretical background and the methodology. We review how to relate thermal, harmonic fluctuations with the (effective) spring constants of the underlying eigenmodes. Included is also a brief description of how to generate the full force constants matrices $\Phi_{\alpha\beta}(\mathbf{q})$ if their leading-order expansion coefficients are known as well as a discussion of how quickly GFMD converges compared to all-atom simulations. In Sec. III, GFMD will be applied to calculate the elastic force constants of various two- and three-dimensional lattices. These results can be seen as an initial step to construct a library of the expansion coefficients of semi-infinite solids. Comparison of the numerically obtained coefficients is made to analytical expressions, whenever we are aware of exact solutions. In Sec. IV, GFMD is applied to various nonadhesive contact mechanics models, i.e., the exactly solved Hertzian contact as well as the approximately solved complete contact between a rigid, self-affine substrate and an elastic manifold. Last, a harmonic solid is pressed against a substrate whose roughness was experimentally determined. Conclusions are drawn in Sec. V.

II. THEORY AND METHODOLOGY

A. Thermal fluctuations and renormalization of harmonic variables

In this section, some properties of harmonic variables are briefly reviewed. It will be shown how integrating out harmonic variables in the partition function renormalizes the coupling between the remaining, explicitly represented harmonic degrees of freedom. None of this material is new.[26] For example, conceptually similar approaches have been used to calculate thermal displacements of surface atoms in nickel[27] and the underlying ideas can be extended to include anharmonic corrections of thermal displacements in the bulk.[19] However, a brief and focused overview might prove useful to readers who are not familiar with Gaussian integrals in statistical mechanics.

Consider a system of bilinearly coupled degrees of freedom $\{u\}$, for which the potential energy V is given by

$$V = \sum_{i,j} \frac{1}{2} k_{ij} u_i u_j \tag{1}$$

with the regular choice of $k_{ij}=k_{ji}$. The coefficients, or spring constants, k_{ij} must form a positive-definite matrix $\mathbf{k}$ for mechanically stable solids. (Zero eigenvalues of this matrix would be associated with translation and rotation of the solid, which we do not intend to consider here.) In thermal equilibrium, the u_i's will be distributed according to the Boltzmann statistics, i.e., the probability to find a given configuration will be proportional to $\exp(-\beta V)$, where $\beta=1/k_BT$ is the inverse thermal energy.

By expressing the u_i and du_i in terms of the eigenvectors of the $\mathbf{k}$ matrix, it is easy to show that the second moments of the displacements u_i satisfy

$$\langle u_i u_j \rangle = \frac{1}{Z(\beta)} \int du_1 \cdots du_N u_i u_j e^{-\beta V} = k_B T [\mathbf{k}^{-1}]_{ij}, \tag{2}$$

where the partition function $Z(\beta)$ is given by

$$Z(\beta) = \int du_1 \cdots du_N e^{-\beta V}. \tag{3}$$

Suppose now that $\mathbf{k}$ is unknown, but that there is a sufficiently large number of observations of $\{u\}$ in thermal equilibrium so that all $\langle u_i u_j \rangle$ are known to great accuracy. One can then use Eq. (2) to reconstruct the $\mathbf{k}$ matrix.

Alternatively, if one knows the forces F_i on unit i, then the $\mathbf{k}$ matrix can be reconstructed directly, provided the set

$\{F\}$ is known for N linearly independent configurations $\{u\}$, i.e., the k_{ij} must satisfy

$$F_i = \sum_j k_{ij} u_j \tag{4}$$

for every single set $\{u\}$. In conclusion, when monitoring the correlation matrix $\langle u_i u_j \rangle$ or a sufficiently large set of forces $\{F\}$ and displacements $\{u\}$, it is possible to reconstruct the elastic interactions.

A useful property of harmonic systems is that integrating out individual degrees of freedom leaves the Boltzmann factor of the remaining terms in a Gaussian form, i.e.,

$$\int du_n e^{-\beta V} \propto e^{-\beta \tilde{V}'}, \tag{5}$$

where

$$\tilde{V}' = \frac{1}{2} \sum_{i \neq n, j > i; j \neq n} \tilde{k}_{ij} u_i u_j \tag{6}$$

and

$$\tilde{k}_{ij} = k_{ij} - k_{in} k_{jn} / k_{nn}. \tag{7}$$

The coefficients $\tilde{k}_{ij}$ can be considered to be effective or renormalized spring constants. It is important to mention that the proportionality factor in Eq. (5) does not depend on any displacement variable. This means that we can use Eq. (2) also for evaluation of renormalized effective spring constants.

In principle, many harmonic variables can be eliminated according to the scheme outlined in Eqs. (5)–(7), i.e., those degrees of freedom that do not couple directly to any *external* force. In the given context of a semi-infinite elastic solid in contact with an adsorbate or a substrate, it will be reasonable to assume that only the first or the first few layers interact with the adsorbate and/or substrate, respectively. All layers beyond the "interaction zone" can be included in a single Green's function layer.

While it is possible to use Eq. (2) for the calculation of effective elastic couplings $\tilde{k}$, it is not possible to use Eq. (4) without further modification for the same purpose. The reason is that the forces F_i are fluctuating quantities and Eq. (4) only holds on average.

Thus, we need to identify those $\tilde{k}_{ij}$ that minimize the error function χ^2 defined as

$$\chi^2 = \left\langle \left(F_i - \sum_j \tilde{k}_{ij} u_j \right)^2 \right\rangle, \tag{8}$$

where the indices on the right-hand side of the last equation and the following equations only run over those degrees of freedoms that are not integrated out. Note that taking the expectation value requires sampling of the whole system, including the variables that will be eliminated. Minimizing χ^2 with respect to $\tilde{k}_{ij}$ yields

$$\tilde{k}_{ij} = \sum_n \langle F_i u_n \rangle (\mathbf{G}^{-1})_{nj}, \tag{9}$$

where the coefficients G_{ij} of the matrix $\mathbf{G}$ are defined as

$$G_{ij} = \langle u_i u_j \rangle. \tag{10}$$

When computing the $\tilde{k}_{ij}$'s, Eq. (9) promises to be less susceptible to statistical errors than Eq. (2), for example, when applied to a single harmonic degree of freedom, Eq. (9) is exact for a single configuration (unless the system happens to sit in the potential energy minimum), while determining the spring constant with the help of Eq. (2) would require sampling of many configurations.

If the remaining degrees of freedom, i.e., those that have not been integrated out, are coupled to an external potential V_{ext}, one can say that the remaining atoms move on a (average) potential V given by

$$V = \sum_{i,j} \frac{1}{2} \tilde{k}_{ij} u_i u_j + V_{\text{ext}}(\{u\}). \tag{11}$$

B. Representation of elastic coupling in periodic systems

The procedure to eliminate harmonic degrees of freedom, presented in the preceding section, applies to periodic and nonperiodic systems alike. However, the representation of effective interactions in periodic systems can be made sparse by exploiting the translational symmetries of the semi-infinite crystal. Instead of calculating effective spring constants between individual (surface) atoms in real space, it is more efficient to assess the effective elastic coupling in reciprocal space, because modes with different wave number cannot couple in the harmonic approximation for symmetry reasons. Thus, if $\mathbf{u}_n$ is a displacement vector of atom n with equilibrium position $\mathbf{R}_n^0$ in real space and its Fourier transform is defined as

$$\tilde{\mathbf{u}}(\mathbf{q}) = \frac{1}{\sqrt{N}} \sum_n \mathbf{u}_n \exp(i\mathbf{q}\mathbf{R}_n^0), \tag{12}$$

then, the only terms to be averaged are

$$G_{\alpha\beta}(\mathbf{q}) = \langle \tilde{u}_\alpha^*(\mathbf{q}) \tilde{u}_\beta(\mathbf{q}) \rangle, \tag{13}$$

which replace the G_{ij}'s in Eq. (10). Note that the $\mathbf{q}$'s have the dimensionality of the interface, i.e., typically two components, say x and y, while the $\mathbf{u}$'s are vectors with all three Cartesian coordinates.

For three-dimensional simple solids with N atoms in the interface one would have to accumulate and diagonalize a Green's function matrix of dimension $(3 \cdot N) \times (3 \cdot N)$ if no use were made of periodicity. Conversely, making use of periodicity only requires the observation and diagonalization of N matrices of dimension 3×3. Note that for crystals with basis, the indices in $G_{\alpha\beta}$ would incorporate the Cartesian coordinates of all atoms in the unit cell. This unit cell only needs to be the unit cell of the very bottom layer and can therefore be smaller than the unit cell of the whole three-dimensional structure.

As is the case for other harmonic systems, the inverse of a correlation matrix $\mathbf{G}$ divided by the thermal energy can be

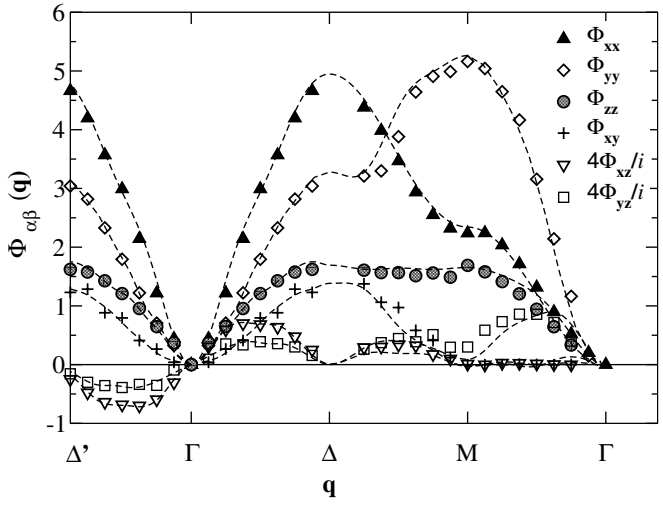

FIG. 1. Dispersion of the surface stiffness coefficients for a semi-infinite (111) surface of an fcc lattice. Some components of the $\Phi_{\alpha\beta}(\mathbf{q})$ matrix are multiplied by a factor of 4 for reasons of optical resolution. The lines correspond to fits whose adjustable parameters are given in Sec. III.

interpreted as effective elastic interactions $\Phi_{\alpha\beta}(\mathbf{q})$ in reciprocal space, i.e.,

$$\Phi_{\alpha\beta}(\mathbf{q}) = \beta[\mathbf{G}^{-1}(\mathbf{q})]_{\alpha\beta}. \tag{14}$$

The symmetry properties of functions defined in reciprocal space facilitate their representation. To be specific, the $\Phi(\mathbf{q})$ matrices only need to be known in the first Brillouin zone, because they are periodic in the reciprocal lattice. In theory this means that the components of the $\Phi(\mathbf{q})$'s can be written as a Fourier series,

$$\Phi_{\alpha\beta}(\mathbf{q}) = \sum_{\Delta\mathbf{R}} \tilde{\Phi}_{\alpha\beta}(\Delta\mathbf{R}) e^{i\mathbf{q}\Delta\mathbf{R}}, \tag{15}$$

where the $\tilde{\Phi}(\Delta\mathbf{R})$ are expansion coefficients and the $\Delta\mathbf{R}$ are the reciprocal lattice vectors of the reciprocal lattice, that is, the original lattice vectors.

For the three-dimensional lattices studied here, it appears that the $\Phi_{\alpha\beta}(\mathbf{q})$'s are either real and symmetric functions of $\mathbf{q}$ with a cusp at the Γ point, namely Φ_{xx}, Φ_{yy}, and Φ_{zz}, or they are real and antisymmetric, i.e., $\Phi_{xy}(\mathbf{q}) = -\Phi_{xy}(-\mathbf{q})$, or purely imaginary and antisymmetric, Φ_{xz}, Φ_{yz}. An example for the dispersion of the stiffness matrix is shown in Fig. 1. Details of the calculations are presented in Sec. III. Due to the symmetry properties of the $\Phi_{\alpha\beta}$, it is convenient to represent the $\Phi(\mathbf{q})$ matrix in the following way:

$$[\Phi_{\alpha\beta}] = \begin{bmatrix} \Phi_{xx} & 0 & 0 \\ 0 & \Phi_{yy} & 0 \\ 0 & 0 & \Phi_{zz} \end{bmatrix} + \begin{bmatrix} 0 & \Phi_{xy} & 0 \\ \Phi_{xy} & 0 & 0 \\ 0 & 0 & 0 \end{bmatrix} + i \begin{bmatrix} 0 & 0 & +\Phi_{xz}/i \\ 0 & 0 & +\Phi_{yz}/i \\ -\Phi_{xz}/i & -\Phi_{yz}/i & 0 \end{bmatrix} \tag{16}$$

Some of the components of the $\Phi(\mathbf{q})$ matrix, that is, only those on the diagonal, would not yield quickly converging series if they were written as a simple Fourier sum. The reason is that they have a cusp in the center of the Brillouin zone, which is similar to that of a phonon dispersion $\omega(\mathbf{q})$. The slow convergence of the $\Phi_{\alpha\beta}(\mathbf{q})$'s when expressed as a Fourier series can be overcome if the squares of those $\Phi_{\alpha\beta}(\mathbf{q})$'s are written as a Fourier series rather than their first moments, i.e.,

$$\Phi^2_{\alpha\beta}(\mathbf{q}) = \sum_{\Delta\mathbf{R}} \tilde{\Phi}^{(2)}_{\alpha\beta}(\Delta\mathbf{R}) e^{i\mathbf{q}\Delta\mathbf{R}}, \tag{17}$$

where the $\tilde{\Phi}^{(2)}_{\alpha\beta}(\Delta\mathbf{R})$'s are the expansion coefficients of the squared elastic coupling terms. Note that one shall not employ summation convention on the left-hand side of Eq. (17).

The representation of the elastic interactions in terms of the Fourier series Eqs. (15) and (17) is quickly converging for quickly decaying potentials. It turns out that only those expansion coefficients $\tilde{\Phi}_{\alpha\beta}(\Delta\mathbf{R})$ and $\tilde{\Phi}^{(2)}_{\alpha\beta}(\Delta\mathbf{R})$ need to be included for which $\Delta\mathbf{R}$ is a lattice vector connecting a central particle with a nearest or next-nearest neighbor. Exceptions are the simple square (ss) and the simple cubic (sc) lattice, which require (strong) interactions between next-nearest neighbors for reasons of mechanical stability.

Besides the translational symmetries of the crystals, there are also point symmetries, which further reduce the number of independent expansion coefficients. If the expansion coefficient $\tilde{\Phi}_{\alpha\beta}(\Delta\mathbf{R})$ is known for say, $\Delta\mathbf{R} = (1,0,0)a$, where a is the nearest-neighbor distance, and the rotation matrix $\mathbf{U}$ maps $\Delta\mathbf{R}$ to an equivalent neighbor $\Delta\mathbf{R}' = \mathbf{U}\Delta\mathbf{R}$, then this same rotation matrix can be used to map $\tilde{\Phi}_{\alpha\beta}(\Delta\mathbf{R})$ onto $\tilde{\Phi}_{\alpha\beta}(\Delta\mathbf{R}')$.

To illustrate how the point symmetries can be used in a sparse representation of the elastic interactions, we discuss the two-dimensional hexagonal lattice, which is formed by the surface atoms in the (111) surface of a face-centered-cubic (fcc) lattice and also by the (001) surface of the three-dimensional hexagonal closed-packed lattice. The rotation matrices can be written as

$$\mathbf{U} = \begin{pmatrix} \cos(n\pi/3) & \sin(n\pi/3) & 0 \\ -\sin(n\pi/3) & \cos(n\pi/3) & 0 \\ 0 & 0 & 1 \end{pmatrix}, \tag{18}$$

where $0 \leqslant n \leqslant 5$ is an integer number. If $\Delta\mathbf{R}$ is a lattice vector, then so is $\Delta\mathbf{R}' = \mathbf{U}\Delta\mathbf{R}$ and the components of the expansion coefficient associated with $\Delta\mathbf{R}'$ read

$$\tilde{\Phi}(\Delta\mathbf{R}') = \mathbf{U}^{\mathbf{T}} \tilde{\Phi}(\Delta\mathbf{R}) \mathbf{U}. \tag{19}$$

A similar relationship holds for the transformation of the matrix $\tilde{\Phi}^{(2)}(\Delta\mathbf{R}')$.

It is important to realize that Fourier expansion coefficients such as $\tilde{\Phi}^{(2)}_{xy}(\Delta\mathbf{R})$ are not necessarily identical to zero, although the sum over all symmetry-related terms vanishes. The knowledge of $\tilde{\Phi}^{(2)}_{xy}(\Delta\mathbf{R})$ is required, because such an off-diagonal term can become diagonal through the symme-

try operation defined in Eq. (19). The nonzero expansion coefficients are $\tilde{\Phi}^{(2)}_{xx}$, $\tilde{\Phi}^{(2)}_{yy}$, $\tilde{\Phi}^{(2)}_{zz}$, $\tilde{\Phi}^{(2)}_{xy}$, $\tilde{\Phi}^{(2)}_{yz}$, $\tilde{\Phi}^{(2)}_{xz}$, which are needed for the reconstruction of the first term on the right-hand side of Eq. (16) as well as $\tilde{\Phi}_{xy}$, and $\tilde{\Phi}_{xz}$, $\tilde{\Phi}_{yz}$, which reconstruct the second and third term on the right-hand side of Eq. (16), respectively. Each of the stated coefficients is either real or purely imaginary.

In conclusion, the effective interactions of surface atoms can be expressed in reciprocal space. The $\Phi_{\alpha\beta}(\mathbf{q})$ are periodic in the reciprocal lattice and they or their squares can thus be represented as a Fourier series. The Fourier expansion coefficients $\tilde{\Phi}_{\alpha\beta}(\Delta\mathbf{R})$ or $\tilde{\Phi}^{(2)}_{\alpha\beta}(\Delta\mathbf{R})$ only need to be known for one atom per neighbor shell. All symmetry equivalent coefficients can be obtained by applying rotation matrices that map the surface onto itself. In Sec. III, tables will be listed for various simple crystalline structures.

C. Model for the interaction between a substrate and a slider

For frictionless contacts, it is possible to map the contact mechanics of two elastic solids each being rough onto that of a flat, elastic solid and a rigid, rough solid.[28] We will use this isomorphism, because the applications in this work are solely concerned with contact mechanics. In the following, a flat, discrete, semi-infinite, elastic lattice will be pressed against a continuous, rigid, rough substrate.

The rigid substrate will be defined by a *continuous* height function $h(x)$. For three-dimensional systems, the height function $h(\mathbf{r})$ depends on the in-plane vector $\mathbf{r}=(x,y)$. Using continuous height functions makes it possible to test continuum-mechanics predictions more easily than if the substrate were composed of discrete atoms, in which case it was found that continuum mechanics can break down.[29] It is yet possible to investigate the effect of discreteness within GFMD, e.g., by adding significant roughness to the substrate at a wavelength near the discretization of the elastic slider.

In test simulations of Hertzian contacts, the height function was chosen to be circular, i.e.,

$$h(x) = (R^2 - x^2)^{1/2}\Theta(R - |x|)$$

for one-dimensional interfaces, or spherical

$$h(\mathbf{r}) = (R^2 - r^2)^{1/2}\Theta(R - r)$$

for two-dimensional interfaces. In both cases, R denotes the radius of curvature as specified in Hertzian contacts and $\Theta(\bullet)$ is the Heaviside step function, defined as unity for positive and zero for negative arguments. In our computations, the indentation depth was kept small compared to the linear size of the periodically repeated cell and the substrate's radius of curvature so that the spherical cap was equivalent to a parabolic tip, for which Hertzian contact mechanics is exact.

The simulation of Hertzian contacts was important to ascertain at what level of spatial discretization (lattice constant a divided by contact radius R_c), it is possible to obtain accurate pressure histograms $P(p)$. Pressure histograms are helpful in a meaningful determination of the true contact area in the case of randomly rough substrates.

Randomly rough surfaces were considered as well. Their topology is often characterized by a height-difference correlation function $C_2(r)$ defined as

$$C_2(r) = \langle \{h(0) - h(r)\}^2 \rangle. \tag{20}$$

Sometimes, we produced these functions using a Fourier filtering algorithm,[30] while in other simulations, an experimental height map was taken as input. For the artificially generated functions $h(x)$ or $h(\mathbf{r})$, the surface was represented in reciprocal space and the values for the Fourier transform[30] $\tilde{h}(q)$ of $h(x)$ were chosen such that

$$\langle \tilde{h}^*(q)\tilde{h}(q) \rangle = h_s^2 (q/q_s)^{-2H-D_{\mathrm{int}}}\Theta(q - q_s)\Theta(q_l - q), \tag{21}$$

where h_s is a Gaussian random variable with zero mean and a standard deviation that represents the fluctuation of the height profile associated with the short-wavelength cutoff q_s. D_{int} is the dimensionality of the interface, e.g., $D_{\mathrm{int}}=2$ for three-dimensional solids and H is the so-called Hurst roughness exponent. q_s and q_l denote cutoffs for roughness at short and long wavelengths, respectively. In the limit of $q_s=0$ and $q_l \to \infty$, $C_2(r)$ scales algebraically with r^{2H}.

To fully determine the contact mechanics, interactions between the two opposed surfaces must be specified. In most simulations, hard walls potentials are employed, i.e., if the z coordinate of atom n at position x crosses through $h(x)$, the interaction energy increases from zero to infinity. As long as one is not interested in the detailed dynamics of the slider but only in static (zero-temperature) properties, these hard-wall potentials can be implemented by using regular molecular dynamics, in which external and intraslider forces act on atom n. The boundary condition $z_n \geqslant h(x_n)$ can be enforced at the end of each time step by setting z_n to $h(x_n)$ if the "predicted" value of z_n turned out less than $h(x_n)$.

For studies of dynamical phenomena, hard-wall interactions are not straightforward to implement. This is one of the reasons why in some cases, the interaction between substrate and the elastic manifold was modeled with an exponentially repulsive potential[31]

$$V(z_n) = V_0 \exp\{-[z_n - h(x_n)]/\sigma\}, \tag{22}$$

where V_0 and σ are constants of unit energy and length, respectively. In the limit $\sigma \to 0$, $V(z_n)$ mimics hard walls potentials. Even at finite values of σ, the ratio of lateral and normal forces has the "hard-wall property" that the lateral and normal force are proportional to each other, the local slope of $h(x)$ being the proportionality coefficient. Thus, the precise value of V_0 has no effect on the wall-manifold potentials other than shifting the slider's center of mass. The parameter σ is adjustable. To make the exponential walls look similar to hard walls, it is desirable to choose σ as small as possible. However, for computational convenience, large values of σ are preferred. Small σ's can limit the MD time step significantly, because normal forces alter quite quickly when slider atoms approach the substrate. We found $\sigma=a/4$, which is our default choice for σ unless mentioned otherwise, to be a good compromise between the two opposed requirements. Moreover, if we took a to be the spacing of a covalent bond or a typical nearest-neighbor distance in a molecular solid,

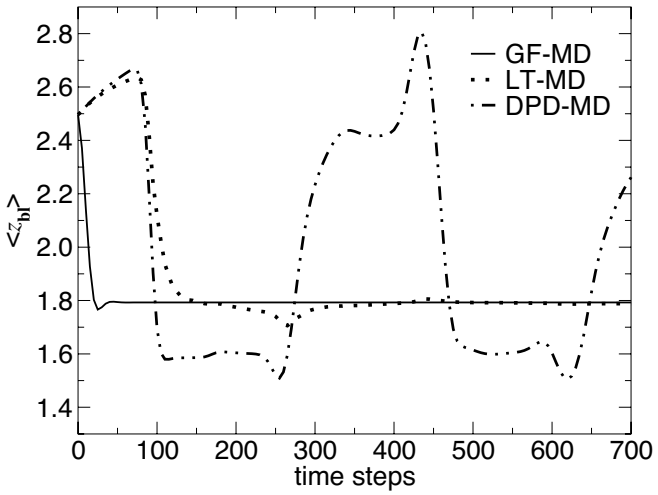

FIG. 2. Normal center-of-mass position of the bottom layer $\langle z_{\mathrm{bl}} \rangle$ of a square solid ($N=256\times256$ atoms) as a function of the number of time steps for different MD integration schemes: Green's function molecular dynamics (GFMD, solid lines), MD of whole elastic manifold thermostatted with Langevin thermostat (LT-MD, broken lines), MD of whole elastic manifold with dissipative particle dynamics thermostat (DPD-MD) (Ref. 34). Time steps were chosen identical in each case, and the strength of the thermostat was optimized for each individual MD technique to minimize the convergence rate.

then the choice of $\sigma=a/4$ would be reasonably close to the real values used in, for instance, Morse or Buckingham potentials.

Besides the hard-wall property, $F_x=\nabla h(x)F_z$, another feature of the exponential interactions seems appealing: Repulsion in real materials is due to the Pauli exclusion principle.[32] As the density of closed-electron shell systems decays approximately exponentially, Eq. (22) mimics true repulsion between atoms in a very crude fashion. Large values of σ relative to spacing (e.g., fluorine atoms terminating dangling bonds in a carbon chain as in teflon) mean smaller effective roughness than small values of σ (e.g., hydrogen atoms terminating dangling bonds).

D. Comments on the dynamics and the convergence rate of GFMD

When performing molecular dynamics simulations of semi-infinite regular lattices, it is desirable to have an algorithm at hand, which not only works correctly but also works fast, because such algorithms allow one to study longer time and length scales. Therefore it is interesting to investigate how quickly an elastic manifold that is initially placed above a substrate and then pressed down at a specified normal load reaches its mechanical equilibrium.

Different dynamical schemes, which all yield the same equilibrium configuration, were tested regarding their rate of convergence, and the results are shown in Fig. 2. To be specific, we include data of GFMD, where individual atoms are damped via a Langevin thermostat and *all-atom simulations* where the thermostat was either a Langevin thermostat[33] (LT) or a dissipative-particle dynamics[34] (DPD) thermostat. In Langevin thermostats, a friction term and a stochastic random noise act in the "laboratory system," which ensures the canonical distribution in the absence of external driving and sufficiently long waiting time. DPD is similar to Langevin, however, friction and random noise always act on (interacting) pairs of atoms such that the center-of-mass motion of this pair is not affected, which conserves their net momentum. DPD has proved to be extremely valuable in simulations of fluids or gasses, because it properly reproduces hydrodynamic interactions. Note that the choice of temperature has no effect on the rate of convergence in these calculations.

The three investigated numerical schemes reveal quite different convergence rates. GFMD already equilibrates reasonably well within 20 MD time steps. This anticipates that convergence is affected only marginally by system size. Langevin thermostat based all-atoms simulations equilibrate much more slowly, while DPD based all-atom molecular dynamics equilibrates prohibitively slow for large systems. The slow convergence in the Langevin-based calculations can be understood as follows: Information must travel from the top of the manifold that experiences the normal load to the bottom surface, which initially overlaps partially with the substrate—hence the positive slope in $z_{\mathrm{bl}}(t)$. Conversely, the Green's function layer experiences both forces right from the start. The extremely bad convergence of the DPD all-atom simulations can be understood from the fact that damping in reciprocal space is inversely proportional to wavelength. This gives the system little chance to dump energy into the thermostat or damping term. When the substrate is extremely rough on large length scales, then individual atoms need to travel long distances, which leads to a less favorable size scaling in each of the three approaches.

The improvements in real computing time owing to GFMD are even more dramatic than what can be inferred from Fig. 2. In that figure it was not taken into account that GFMD only requires to step forward in time the surface atoms, i.e., approximately $(L/a)^{D_{\mathrm{int}}}$ operations, while the other two simulations techniques require $(L/a)^{D_{\mathrm{int}}+1}$ operations. Thus including the results from Fig. 2, the combined benefit of GFMD over *all-atom* LT-MD is approximately $(L/a)^2$ divided by a correction logarithmic in the number of particles taken into account.

It may also be useful to compare the computational efficiency of GFMD to coarse-grained techniques (CGTs). In CGTs the computational effort of a single time step is only $\mathcal{L}^2$ rather than $\mathcal{L}^2 \ln \mathcal{L}$ as in GFMD. However, in CGTs several dozen times $\ln \mathcal{L}$ time steps will have to pass by before information between the (coarse-grained) top plate and bottom layer can be exchanged. This argument makes the favorable assumption that good transmission of sound waves with mass-matching techniques can be achieved.[8,11] Thus, in theory, both approaches scale with $\mathcal{L}^2 \ln \mathcal{L}$, however, we feel that the prefactors are smaller for GFMD.

As mentioned in the introduction, it is possible to generalize the GFMD approach to time-dependent Green's functions in a way such that not only the static properties are reproduced but also the dynamics.[20] Unfortunately, different wave numbers can couple dynamically, i.e., the time-dependent Green's function

$$G_{\alpha\beta}(\mathbf{q},\mathbf{q}',\Delta t) = \langle \tilde{u}^*_\alpha(\mathbf{q},t+\Delta t)\tilde{u}_\beta(\mathbf{q}',t)\rangle \tag{23}$$

are not diagonal in $\mathbf{q}$. This breaks the sparseness of the interactions and hence the computational gain due to discretization if the current scheme were applied not only to statics but also to dynamics. Even if an efficient way could be found to incorporate time-memory functionals into the Green's function treatment as suggested a long time ago,[14,15] the coupling of different $\mathbf{q}$ modes appears to render a dynamic GFMD into an order $\mathcal{L}^{2D_{\rm int}}$ procedure. Potentially another factor of $\mathcal{L}$ enters the computational cost of dynamic GFMD due to the bookkeeping of the past history of the modes. Thus, one may conclude that the computational expense of static GFMD scales with $\mathcal{L}^{D_{\rm int}}$, while dynamic GFMD would scale with $\mathcal{L}^{2D_{\rm int}+1}$, where $D_{\rm int}$ is the dimension of the hypersurface, typically $D_{\rm int}=2$. Even if dynamic GFMD can be made more efficient than projected here, it appears to be a challenge to maintain the favorable $\mathcal{L}^{D_{\rm int}}$ scaling inherent to the static GFMD.

Since an MD simulation based on the static Green's function finds the proper equilibrium configuration rather quickly, i.e., faster than with natural dynamics, it may well be that GFMD gives satisfactory answers to some dynamical processes as well, in particular for quasistatic sliding or small-velocity sliding. At large velocities, however, the GFMD surfaces probably deform too quickly, because momentum transfer is extremely fast. Simulations based on coarse-graining techniques in real space suffer from the inverse problem: Sound waves reflect to a large extent at the boundaries between different levels of discreteness unless special precaution is taken.[19] This reflection artificially slows down the flow of energy and momentum.

III. ELASTIC GREEN'S FUNCTION FOR SELECTED, SEMI-INFINITE SOLIDS

In this section, we will present some results for the matrix of stiffness coefficients for selected (1+1)- and (2+1)-dimensional systems. Our study includes an analysis of finite-size effects and a demonstration that GFMD is indeed able to reproduce the correct contact mechanics.

A. Square lattice with next-nearest-neighbor coupling

The first geometry considered is the two-dimensional, simple square (ss) lattice, in which nearest neighbors are separated by a distance $a=1$ and coupled through a harmonic potential V of the form

$$V = \frac{1}{2}\sum_{i,j>i} k_{ij}[(\mathbf{u}_i - \mathbf{u}_j)\cdot\mathbf{n}_{ij}]^2, \tag{24}$$

where $\mathbf{u}_i$ is the displacement of atom i from its equilibrium position and $\mathbf{n}_{ij}$ is the unit vector parallel to the ideal lattice vector connecting atoms i and j. The stiffness k_{ij} for nearest neighbors is chosen to be $k_1=2$. Next-nearest neighbors are coupled in a similar fashion, however, the stiffness was chosen to be $k_2=1$.

The connection to continuum mechanics of our model[16] can be made by introducing the Eulerian strain tensor $u_{\alpha\beta}$ $=(\partial u_\alpha/\partial R_\beta+\partial u_\beta/\partial R_\alpha)/2$ and by expressing the continuum potential energy as

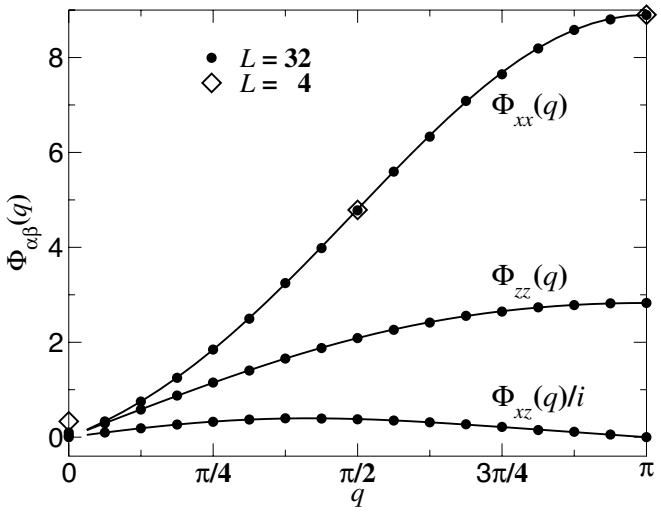

FIG. 3. Stiffness coefficients of the semi-infinite simple square lattice as a function of wave number q. Straight lines are results from analytical calculations (Ref. 16).

$$V = \int dx \int dy \left(\frac{k_1+k_2}{2}(u_{xx}^2+u_{yy}^2) + k_2 u_{xx}u_{yy} + 2k_2 u_{xy}^2 \right). \tag{25}$$

Following the argument in Refs. 16 and 35 this choice of k_1 and k_2 results in Young modulus and Poisson ratio of $E=2.66$ and $\nu=1/3$, respectively. Note that nonpositive values of k_2 for simple-cubic solids do not lead to mechanically stable systems. With the current choice of k_2, the same continuum elastic properties are obtained as for the simple hexagonal lattice with nearest-neighbor coupling $k_1=4/\sqrt{3}$, which will be investigated further below. Moreover, we can compare the matrix coefficients $\Phi_{\alpha\beta}$ obtained numerically with our procedure to an analytical solution given in Ref. 16.

As mentioned in the preceding section, the $\Phi_{\alpha\beta}(\mathbf{q})$ are calculated by averaging in reciprocal space the displacement fluctuations of surface atoms. For the simple square lattice, the (hyper-) surface consists of a linear chain, whose constituting atoms can oscillate parallel and normal to the interface, i.e., atoms are allowed to fluctuate in x and z direction. (To be consistent with the theory section, we choose the direction normal to the interface to be parallel to the z axis even for two-dimensional lattices.) The results for the stiffness matrix are shown in Fig. 3 for different system sizes. They agree with analytically predicted stiffness coefficients[16] within the stochastic error, except for finite-size effects, which are addressed later on.

Due to the absence of rotational symmetries other than a rotation by π, we choose to express the dispersion relation of the stiffness coefficients as

$$\Phi^2_{\alpha\alpha}(q) = \sum_{n\geqslant 0}(2-\delta_{n0})\tilde{\Phi}^{(2)}_{\alpha\alpha}(n)\cos(nqa), \tag{26}$$

for the diagonal elements (δ_{n0} is the Kronecker symbol) and

TABLE I. Expansion coefficients for the stiffness matrix of the simple square lattice. The data is numerically exact.

n	$\tilde{\Phi}^{(2)}_{xx}$	$\tilde{\Phi}_{xz}/i$	$\tilde{\Phi}^{(2)}_{zz}$
0	+31.2836	±0.0000	+4.1809
1	−19.7458	+0.1912	−2.0132
2	+4.1279	+0.0287	−0.0908
3	−0.0641	+0.0002	+0.0131

$$\Phi_{xz}(q) = \sum_{n \geqslant 0} 2\tilde{\Phi}_{xz}(n)\sin(nqa), \tag{27}$$

for the off-diagonal element $\Phi_{xz}(q)=\Phi^{*}_{zx}(q)$. As the $\Phi_{xz}(q)$ are purely imaginary, one can conclude that $\tilde{\Phi}_{xz}(n) = -\tilde{\Phi}_{zx}(n)$. The leading-order expansion coefficients $\tilde{\Phi}_{\alpha\beta}$ and $\tilde{\Phi}^{(2)}_{\alpha\beta}$ are listed in Table I. It can be noticed that the expansion coefficients $\tilde{\Phi}(n)$ quickly decay to zero with increasing n. This behavior is what makes it possible to determine the expansion coefficients for relatively small systems and to use them later in the simulation of large semi-infinite lattices.

B. Finite-size effects

The system size dependence of the force constants is a crucial aspect that also needs to be addressed. Lower and upper bounds for the stiffnesses can be obtained by comparing the force constants calculated via what we call open and closed-boundary conditions, respectively. When using open boundary conditions, the top layer in the solid is allowed to fluctuate freely, except for its center of mass which is kept fixed during the data acquisition. The displacement fluctuations of the atoms in the bottom layer of an open, finite system must thus be larger than the fluctuations in the thermodynamic (td) limit. This makes the system appear softer. Conversely, if the atoms in the top layer are kept fixed, displacement fluctuations in the bottom layer are suppressed, which "stiffens" the manifold. These arguments can be summarized in the following inequality:

$$\Phi_{\text{open}}(q) \leqslant \Phi_{\text{td-limit}}(q) \leqslant \Phi_{\text{closed}}(q). \tag{28}$$

Thus, the difference between $\Phi_{\text{open}}(q)$ and $\Phi_{\text{closed}}(q)$ is a measure of the system size error. Numerical results for the upper bound in the size error are shown in Fig. 4 for the component $\Phi_{xx}(q=\pi/2)$ of the simple square lattice. Identical random seeds were employed to reduce the stochastic errors when comparing closed and open-boundary conditions.

Given a fixed amount of computational resources, the best procedure is to use relatively small systems and to assess their force constants with open and closed boundaries. The average value gives the best guess. Note that in the center of the Brillouin zone all $\Phi_{\alpha\beta}(q)$ are identical to zero.

C. Two-dimensional, hexagonal lattice

A similar calculation of the force constants as for the simple square lattice in Sec. III A was performed for the hexagonal lattice. In the hexagonal lattice only nearest neighbors are coupled with a force constant $k_1=4/\sqrt{3}$, which results in the same long wavelength elastic properties. The dispersion relations for the $\Phi_{\alpha\beta}(q)$ of simple hexagonal (hxg) lattices turns out to be similar to that of simple square lattices, although the expansion coefficients differ to some degree. They are listed in Table II.

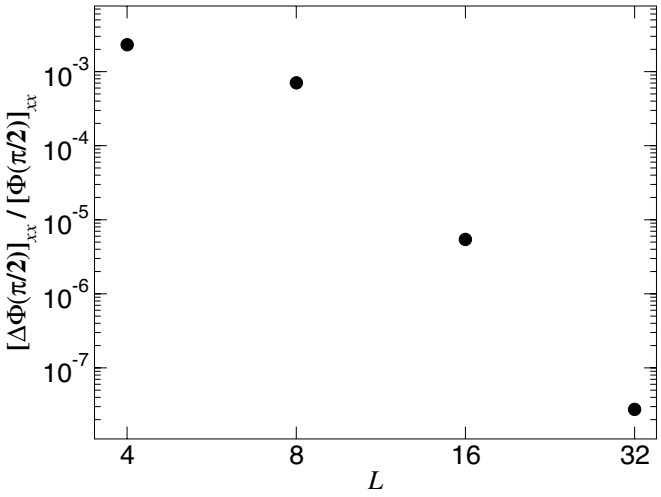

FIG. 4. Difference $\Delta\Phi_{xx}(q=\pi/2)$ in the stiffness coefficient between calculation with a flexible top layer (open) and a rigid top layer (closed), as a function of system size.

To verify the correctness of the numerical values for the coefficients, for which no analytical solutions are known to us, we compared GFMD to all-atom simulations. The results of these computations, in which an elastic manifold is pressed onto a rough substrate can be found in Fig. 5. In that figure, the all-atom simulation is that of a 64×64 system. It is clearly borne out that the GFMD reproduces the contact morphology of the all-atom simulation. The accuracy of GFMD did not deteriorate when the size was increased to 512×512.

D. Three-dimensional lattices

The coefficients for different atomic Bravais lattices in three dimensions can be computed following the same procedure used for the two-dimensional systems. As before, the matrix $\Phi_{\alpha\beta}$ is Hermitian with six independent components as described in Eq. (16). In the following sections, results for the Fourier expansion coefficients for (100) simple-cubic and (111) face-centered cubic (fcc) will be presented.

TABLE II. Expansion coefficients for the stiffness matrix of the hexagonal lattice. The data has ±0.0002 absolute error.

n	$\tilde{\Phi}^{(2)}_{xx}$	$\tilde{\Phi}_{xz}/i$	$\tilde{\Phi}^{(2)}_{zz}$
0	+28.3196	±0.0000	+3.5623
1	−17.9257	+0.1898	−1.8062
2	+3.7409	+0.0116	+0.0212
3	−0.0335	+0.0012	+0.0074

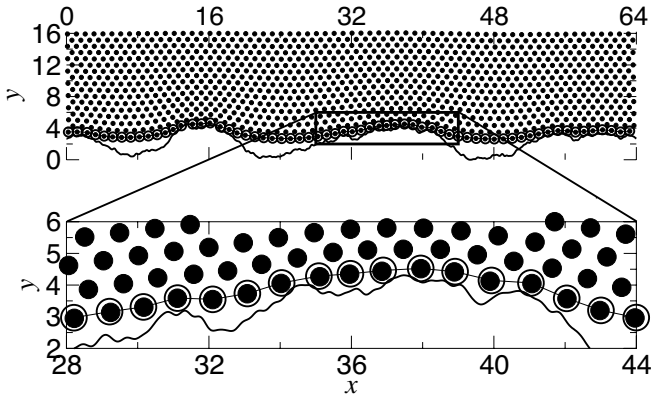

FIG. 5. Comparison of the contact formation of a manifold with a rough substrate: Small, full circles show atomic positions of atoms in the full MD, while large, open circles represent the degrees of freedom used in the GFMD simulations. The lower graph is a magnification of a part of the upper graph.

It may be useful to repeat some of the definitions used in this paper. Whenever spring constants are stated, be it for nearest (k_1) or next-nearest neighbors (k_2), the underlying potential energy function is given in Eq. (24). The Fourier expansion coefficients for the three-dimensional solids are those introduced in Eqs. (15) and (17), which differ from the sine and cosine coefficients for the two-dimensional elastic manifolds used in the preceding section.

1. Simple cubic (100)

While simple-cubic solids are not very common in nature, they constitute good test systems, partially because they are more amenable to analytical calculations. For instance, Saito[17] obtained exact Green's functions for simple-cubic solids of lattice constant $a=1$ with nearest and next-nearest harmonic interactions, $k_1=1$ and $k_2=1$, respectively. This solid has a Young modulus $E=2.43$ and a Poisson ratio $\nu=1/3$.

Here, we intend to demonstrate that our calculations reproduce Saito's exact solutions. Exemplary only the diagonal coefficients of $\Phi_{\alpha\beta}$ are shown in Fig. 6. To represent the matrix element $\Phi_{\alpha\alpha}$ in reciprocal space different paths connecting various symmetry points within the first Brillouin zone were chosen, i.e., those paths that are commonly used to plot phonon dispersion relations. The symmetry points are $\Gamma=(0,0)$, $M=(0,1)\pi/a$, and $\Delta=(1,1)\pi/a$. The agreement between our data and Saito's data is within the numerical error. Similar agreement between our data and Saito's results is found for all off-diagonal elements as well, but not displayed in the graph for reasons of clear visualization, e.g., the cusp of some of the $\Phi_{\alpha\beta}(\mathbf{q})$ is not clearly evident from Fig. 1, while it is more clearly borne out for the $\Phi_{\alpha\alpha}$ in Fig. 6.

Our full results are stated in Table III in terms of the non-vanishing expansion coefficients $\tilde{\Phi}^{(2)}_{\alpha\beta}(\Delta\mathbf{R})$ and $\tilde{\Phi}_{\alpha\beta}(\Delta\mathbf{R})$. For the simple cubic lattice, $\Delta\mathbf{R}$ is represented by the integer numbers n_x and n_y, i.e., if a is the lattice constant, then $\Delta\mathbf{R}=an_x\mathbf{e}_x+an_y\mathbf{e}_y$, where $\mathbf{e}_\alpha$ are unit vectors. Note that the expansion coefficients need to be stated up to the fifth neighbor shell because of the relatively large ratio of k_2/k_1.

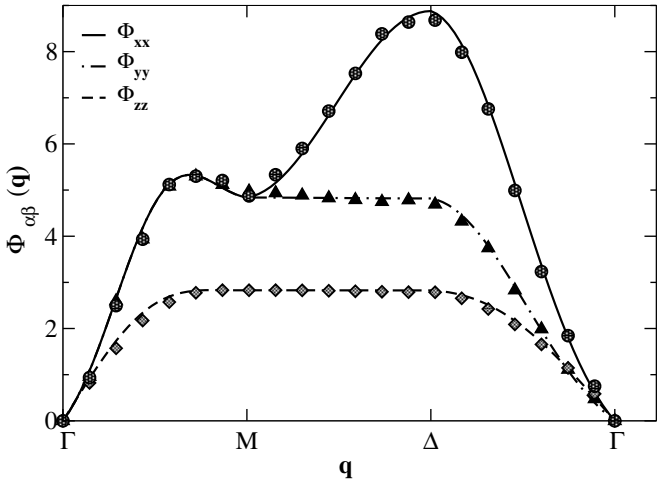

FIG. 6. Numerical (symbols) and analytical (Ref. 17) (lines) results for the diagonal elements of $\Phi_{\alpha\beta}(\mathbf{q})$ in the simple-cubic crystal lattice along lines connecting high symmetry points in the Brillouin zone.

2. Face-centered cubic (111)

No analytical solution of the stiffness matrix for the (111) plane of the fcc lattice is known to us. However, its knowledge may be beneficial, mainly because many metals have thermodynamically stable surfaces with this symmetry.

The (111) plane of fcc lattices has hexagonal symmetry. In order to evaluate the Green's functions $\langle\tilde{u}^*_\alpha(\mathbf{q})\tilde{u}_\beta(\mathbf{q})\rangle/k_BT$, it is useful to label the atoms in such a way that use can be made from fast Fourier transformation techniques in a straightforward fashion. For this purpose, the convention described in Fig. 7 was used.[36] Note that the point symmetry

TABLE III. Expansion coefficients $\tilde{\Phi}^{(2)}_{\alpha\beta}(\Delta\mathbf{R})$ and $\tilde{\Phi}_{\alpha\beta}(\Delta\mathbf{R})$ of the 3D simple-cubic lattice with $k_1=k_2=1$. $\Delta\mathbf{R}=(n_x,n_y)$ for a system with lattice constant $a=1$.

n_x	n_y	$\tilde{\Phi}^{(2)}_{xx}$	$\tilde{\Phi}^{(2)}_{yy}$	$\tilde{\Phi}^{(2)}_{zz}$
0	0	+26.2801	+26.2801	+6.2489
1	0	−9.8853	+1.9890	−0.9663
1	1	−4.9398	−4.9398	−0.5046
2	0	+1.5446	+0.5077	−0.0786
2	1	+1.0296	+0.0048	−0.0205
2	2	+0.2585	+0.2585	+0.0165
n_x	n_y	$\tilde{\Phi}_{xy}=\tilde{\Phi}_{yx}$	$\tilde{\Phi}_{xz}=\tilde{\Phi}^*_{zx}$	$\tilde{\Phi}_{yz}=\tilde{\Phi}^*_{zy}$
0	0	±0.0000	±0.0000*i	±0.0000*i
1	0	±0.0000	+0.0891*i	±0.0000*i
1	1	−0.4552	+0.0475*i	+0.0475*i
2	0	±0.0000	+0.0144*i	±0.0000*i
2	1	+0.0011	+0.0069*i	+0.0032*i
2	2	−0.0028	±0.0000*i	±0.0000*i

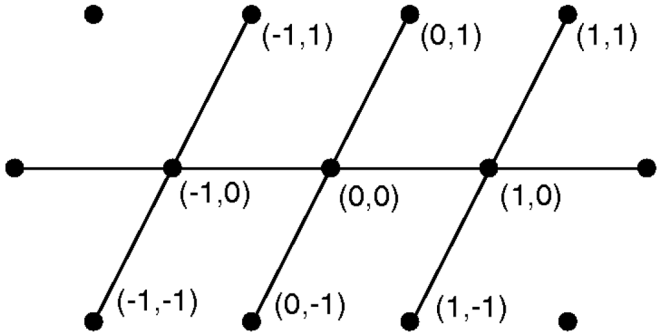

FIG. 7. Labeling scheme of the sites within the hexagonal lattice using integer pairs of numbers (n_x, n_y) according to Ref. 36.

transformation as described in Eq. (19) have to be performed on the real-space coordinates and not on the indices introduced in Fig. 7. As an example, the point $(n_x, n_y)=(1,0)$ maps onto (0,1) under a $\pi/3$ rotation.

The results for the stiffness matrix expansion coefficients are stated in Table IV. The knowledge of the coefficients associated with nearest and next-nearest neighbors yields numerically accurate results. Contributions related to more distant neighboring shells appear to vanish exponentially fast. Due to the similar local atomic arrangements of (111) fcc planes and (001) hexagonal-closed-packed (hcp) planes, the results stated in Table IV are excellent approximations to the effective force constants of (001) hcp surfaces.

TABLE IV. Expansion coefficients $\tilde{\Phi}_{\alpha\beta}(\Delta\mathbf{R})$ for the (111) surface of the fcc lattice. In the full three-dimensional solid, only nearest neighbors were coupled with springs $k_1=1$. The statistical accuracy of the nondiagonal coefficients is only ±0.005.

n_x	n_y	$\tilde{\Phi}_{xx}$	$\tilde{\Phi}_{yy}$	$\tilde{\Phi}_{zz}$
0	0	+3.1079	+3.0001	+1.3971
1	0	−0.9112	−0.1168	−0.1576
1	1	−0.0086	+0.0086	−0.0215
n_x	n_y	$\tilde{\Phi}_{xy}=\tilde{\Phi}_{yx}$	$\tilde{\Phi}_{xz}=\tilde{\Phi}^*_{zx}$	$\tilde{\Phi}_{yz}=\tilde{\Phi}^*_{zy}$
0	0	±0.0000	$\pm 0.0000*i$	$\pm 0.0000*i$
1	0	±0.0000	$+0.0599*i$	$\pm 0.0000*i$
1	1	−0.0271	$+0.0046*i$	$+0.0016*i$
n_x	n_y	$\tilde{\Phi}^{(2)}_{xx}$	$\tilde{\Phi}^{(2)}_{yy}$	$\tilde{\Phi}^{(2)}_{zz}$
0	0	+14.3031	+14.1713	+2.2294
1	0	−5.4953	+0.0893	−0.3827
1	1	+0.3974	+0.2258	−0.0063
n_x	n_y	$\tilde{\Phi}^{(2)}_{xy}=\tilde{\Phi}^{(2)}_{yx}$	$\tilde{\Phi}^{(2)}_{xz}=\tilde{\Phi}^{(2)*}_{zx}$	$\tilde{\Phi}^{(2)}_{yz}=\tilde{\Phi}^{(2)*}_{zy}$
0	0	+0.4917	$\pm 0.0102*i$	$-0.0086*i$
1	0	−0.2412	$+0.0007*i$	$-0.0045*i$
1	1	−0.0030	$+0.0031*i$	$-0.0001*i$

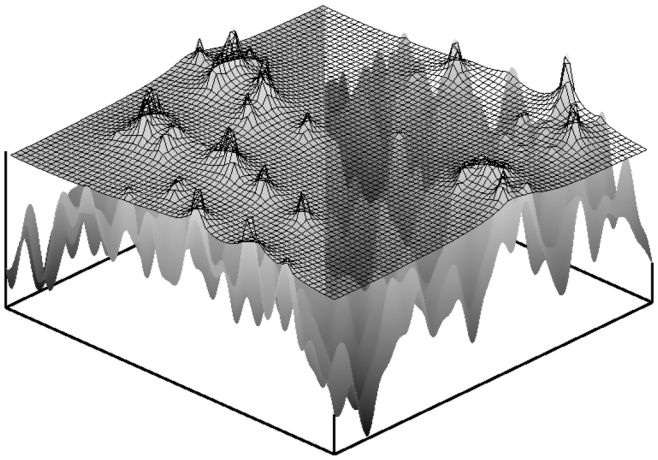

FIG. 8. Illustration of a GFMD configuration representing a three-dimensional, semi-infinite, elastic solid that is pressed against a rigid, self-affine, fractal substrate. The right half of the Green's function layer is represented in a more transparent fashion than the left half. The direction normal to the interface is enlarged approximately 30 times with respect to the in-plane directions.

IV. APPLICATION TO CONTACT MECHANICS

In this section, we will apply our methodology to a variety of contact mechanical problems. This includes a validation of our method for Hertzian contacts, the test of an analytical prediction[24] for the complete contact between an elastic, semi-infinite, flat solid and a self-affine rigid substrate, as well as the analysis of an experimental roughness profile. To illustrate the methodology, a snapshot of a simulation is presented in Fig. 8. Only the shown layer, reminiscent of a membrane, needs to be simulated to yield the contact mechanics of a complete, three-dimensional solid. In all following examples, we used the Green's function of the simple-cubic solid given in Sec. III D 1.

An important observable in the contact mechanical calculations presented below is the normal stress and its probability distribution at the interface between the substrate and the elastic manifold. In the case of hard walls, these quantities can only be obtained indirectly, because of the discontinuous nature of the hard-wall potential. Use can be made of the argument that all forces must balance to zero in mechanical equilibrium. Thus, the force that the impenetrable, rigid substrate exerts on a specific surface atom is equal in magnitude and opposite in direction to the force experienced by the remaining elastic manifold, which is easy to compute. To calculate the local normal pressure, the ratio of the normal force and the area associated with a particle was formed, where a Voronoi construction via Delaunay triangulation was used to estimate the area per atom.

A. Hertzian contact

The Hertzian contact has become a benchmark for numerical solutions of frictionless contact mechanics, see for instance Ref. 37. The reason is that the geometry of the Hertzian contact is relatively simple, the pressure distribution is analytically known, and it contains sharp features, which are

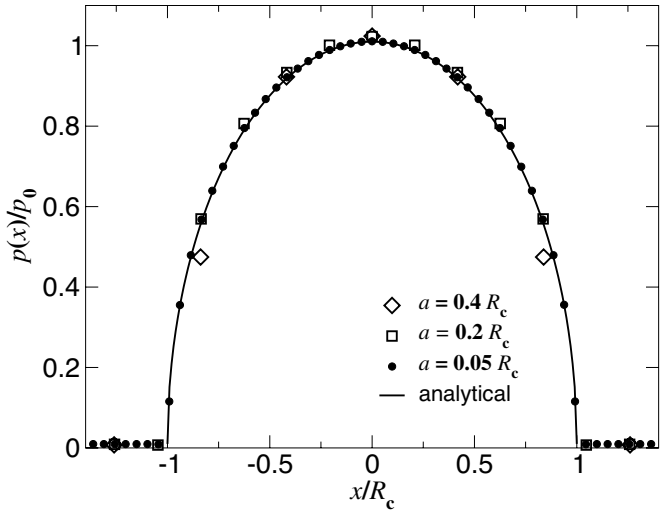

FIG. 9. Pressure profile of a one-dimensional Hertzian contact, i.e., circle on line, in the hard-wall approach for different degrees of discretization of the elastic manifold. The external load was chosen such that in the analytical solution p_0 and R_c are both unity. The linear dimension of the simulations cell was equal to or greater than 200 times the radius of contact. The radius of curvature is not relevant, because only the product of load and radius of curvature matter for $p(x)$.

challenging to obtain numerically. Any numerical scheme should have the ability to reproduce exact solutions within controllable accuracy. Even if it may not always be necessary to achieve the highest accuracy, one should yet be in a position to estimate systematic errors due to, say, finite discretization of the elastic manifold. Under the assumption of no adhesion and no shear stress at the interface, Hertz found that when squeezing a deformable spherical or parabolic tip against a flat, rigid surface, a circular contact is formed and that the pressure profile in the contact area is given by the expression:[28]

$$p(r) = p_0\left[1 - \left(\frac{r}{R_c}\right)^2\right]^{1/2}\Theta(R_c - r). \tag{29}$$

Here, p_0 is the maximum pressure measured at the center of the tip, R_c is the contact radius, and r is the lateral distance of a point in the surface from the tip's center. As before, $\Theta(\bullet)$ is the Heaviside step function and R without index is the radius of curvature. In three dimensions the values of p_0 and R_c are $p_0=3L/(2\pi R^2)$ and $R_c=[3LR/(4E_c)]^{1/3}$, where L is the normal force acting on the tip and $E_c=E/(1-\nu^2)$ is known as the contact modulus. The same formula, Eq. (29), applies to a two-dimensional circle pressed onto a rigid one-dimensional line, in which case the values of p_0 and R_c become $p_0=2L/(\pi R)$ and $R_c=[4LR/(\pi E_c)]^{1/2}$.

In Fig. 9 we compare the pressure profile obtained in a numerical calculation with the exact solution of the one-dimensional Hertzian contact, i.e., a circle pressed against a line. The numerical data matches Hertz' solution very closely. However, one can notice that obtaining good pressure histograms $P(p)$ requires fine numerical meshes, e.g., if the linear length of the mesh is $a=0.4R_c$ the smallest observed pressure is about $0.5p_0$ and thus little information would be obtained for $p \ll p_0$. It has been argued that in order to obtain meaningful $P(p)$'s, the discretization of the mesh should be less than a tenth, preferentially a hundredth of the contact's linear dimension.[38]

Generally, pressure histograms in purely repulsive contacts are useful to determine the real contact area, A_{real}, in particular in the case of hard-wall interactions.[38] The reason for this statement is that whenever no contact exists, the normal pressure is equal to zero. Any positive pressure, however small it may be, indicates contact. Thus, if $P(p)$ is normalized such that

$$\int_{0^+}^{\infty} dpP(p) = 1 \tag{30}$$

then A_{real} can be calculated from

$$\frac{L}{A_{\text{real}}} = \int_{0^+}^{\infty} dppP(p), \tag{31}$$

where the integration limit 0^+ indicates an arbitrarily small but positive number.

Contacts of macroscopic surfaces can be interpreted as the superposition of (correlated) individual Hertzian contacts. Since the pressure profiles $p(r)$ have diverging slopes at the boundary of each individual microcontact, the probability distribution $P(p)$ must disappear as p approaches zero. The same argument holds in the case of multiasperity contacts. A numerical approach should thus use a grid that makes it possible to accumulate pressure distribution functions exhibiting this behavior. Otherwise, that is, if the mesh is not sufficiently fine, the real contact area may be overestimated.[38]

To judge the performance of different levels of discretization, we have analyzed $P(p)$ in a one-dimensional Hertzian contact, see Fig. 10. The exact distribution function can be derived in an analogous way as the density of states of phonons, $g(E)$, which is commonly calculated with the equation $g(E)dE=g(k)dk$ and a given dispersion relation $E(k)$. In our case, the pressure p plays the role of the phonon energy E and the radius r substitutes the momentum k, thus

$$P(p) = D_{\text{int}}\frac{r^{D_{\text{int}}-1}}{R_c^{D_{\text{int}}}}\left|\frac{dp}{dr}\right|^{-1}. \tag{32}$$

The results of $P(p)$ for one-dimensional and two-dimensional contacts are

$$P(p) = D_{\text{int}}\frac{p}{p_0^2}[1-(p/p_0)^2]^{(D_{\text{int}}-2)/2} \tag{33}$$

as shown previously for $D_{\text{int}}=1$ (Ref. 39) and $D_{\text{int}}=2$ (Ref. 8), respectively. Thus, $P(p)$ is simply a linear function for the regular $D_{\text{int}}=2$, sphere on flat contact. Conversely, for the circle on a line, the histogram is initially linear in p and ends in a van-Hove-type singularity at the boundary of the contact. This behavior is clearly borne out in Fig. 10, in particular for a grid whose (linear) mesh size is less than a tenth of the contact radius. Similar statements regarding the convergence of the pressure histogram hold for the two-

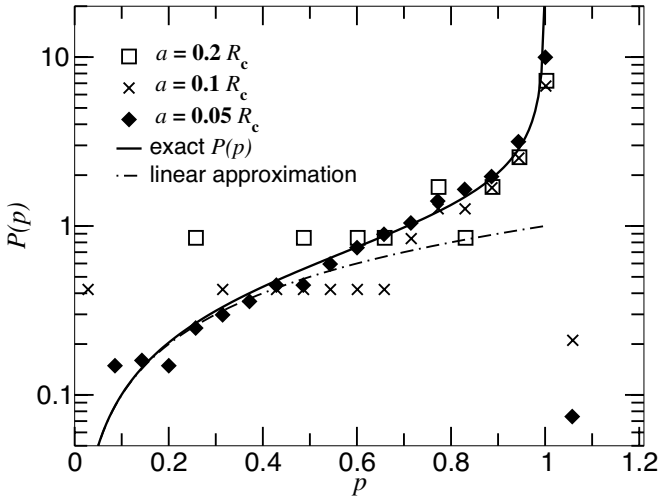

FIG. 10. Pressure distribution $P(p)$ at the interface of the one-dimensional Hertzian contact using the hard walls approach. Different degrees of discretization of the manifold are shown as well as the analytical solution and its linear approximation. Sometimes, $P(p)$ turned out zero in the numerically computed histograms, in which case the data was not included in the graph.

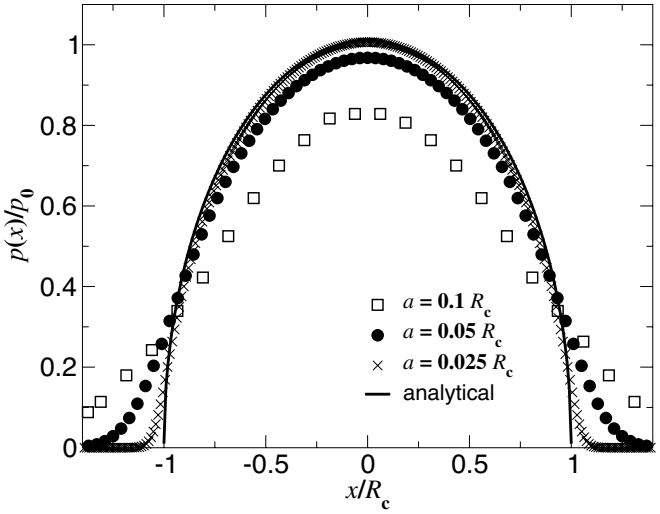

FIG. 11. Normalized pressure profile of a one-dimensional Hertzian contact using the exponential wall interactions with a screening length of $\sigma=0.25a$. Different degrees of discretization of the elastic manifold were used. The radius of curvature of the parabolic tip was chosen to be $128a$, which corresponds to roughly 40 nm if a is a typical interatomic distance of 3 Å. The contact radius R_c was varied by applying different loads.

dimensional Hertzian contact, which is not included explicitly.

Real interactions between surfaces extend over a nonzero distance as opposed to the approximation used within the hard-wall picture, which changes pressure histograms qualitatively. Repulsion between atoms is not hard-wall-like but typically exponential due to the Pauli exclusion principle. Thus, as argued in Sec. II C, the exponential repulsion introduced in Eq. (22) is probably more realistic than hard walls. Replacing hard-wall potentials with more long-ranged interactions eliminates the cusp in $p(r)$ at the (former) boundary of the contact. This can be seen in Fig. 11, where the pressure profiles are shown for different levels of discretization. This in turn alters the distribution function $P(p)$ in such a way that the distribution function $P(p)$ alters its behavior qualitatively at small p, i.e., the delta function contribution stemming from the noncontact areas gets broadened.

We wish to note that other authors in the past have carefully investigated the deviations of pressure distributions between (discrete) atomic systems and continuum mechanics treatments of single-asperity contacts.[8,29] However, the primary interest in Ref. 29 was in identifying effects due to discreteness, commensurability, and atomic arrangements rather than effects due to the finite range of repulsion. Conversely, the analysis in Ref. 8 is much closer in spirit to ours than that in Ref. 29. A technical difference between our work and Ref. 8 is that Yang *et al.* used Lennard-Jones potentials, while we use exponentially repulsive potentials. More importantly, we investigate in more detail how Hertzian contact mechanics becomes increasingly more accurate as the mesh size of the manifold is decreased. Our data reveals that the Hertzian contact profile is rather accurate for a surface curvature typical of atomic force microscope tips, provided that the tips are very smooth. Last, we would like to emphasize that the relevant dimensionless variable is the ratio of σ and R_c, where σ was introduced in Eq. (22). For instance, if we chose $\sigma=2(a/4)$ as opposed to $\sigma=(a/4)$ and set $a=0.025R_c$ instead of $a=0.05R_c$, then the normalized pressure profiles of the two parametrization schemes superimpose almost perfectly.

It is tempting to define contact between two surfaces whenever the distance between them is below a threshold value. However, as outlined in Ref. 8, this leads to discrepancies between Hertzian contacts and estimated contacts whose relative magnitude depends on the local surface curvature. To nevertheless define contact meaningfully, it was suggested to reduce the amount of, we paraphrase, artificially counted contact, such as areas associated with $R>R_c$ in Fig. 11, by comparing numerical data with solutions of appropriate contact mechanical models. It may yet be desirable to define the real contact area merely based on numerically available stress distribution. In some cases, $P(p)$ may go through a minimum at $p=p_{\min}$. If this is the case, it is possible to argue that there is contact for pressures $p \geqslant p_{\min}$, while there is none for $p<p_{\min}$.

B. Flat-fractal contact without adhesion

While Hertzian contact mechanics are well established, there is no generally accepted theory that describes the contact between two surfaces that have roughness on many different length scales. However, recent progress was made towards predicting pressure distributions for elastic contacts in which the original, undeformed surface corrugation can be described as self-affine and randomly rough.[8,24,25,40] Particularly appealing is Persson's theory,[8,24,25] in which it is argued that the pressure distribution in a self-affine contact depends on the level of magnification with which the contact is studied. At small levels of magnification, the pressure distribu-

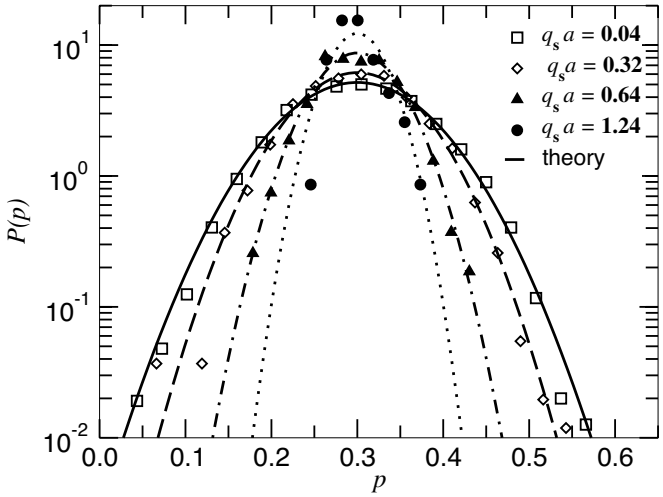

FIG. 12. Pressure distribution for different magnifications at the interface of a rough surface in complete contact with an elastic solid. The distribution is centered at the nominal contact pressure. Full and broken lines are based on a parameter-free theory by Yang *et al.* (Ref. 8).

tion is assessed to be a delta function centered at the nominal contact pressure p_0.

Two cases are generally distinguished, full contact and partial contact. In the case of full contact, predicting the pressure distribution is relatively simple, as the displacement field is essentially defined by the boundary condition. For complete contact and in the absence of adhesion, the pressure histogram must be centered around p_0. While we do not study partial contacts in this section, we wish to note for the next section that in the case of incomplete contact, the pressure distribution peak does not only broaden when the magnification is increased, but the peak also shifts to pressures larger than p_0. Moreover, a new deltalike peak occurs at zero pressure, due to those locations where there is no contact.

In the case of complete contact and at full magnification, Persson's theory predicts a Gaussian pressure distribution,

$$P(p) = \frac{1}{\sqrt{2\pi\sigma_p^2}} e^{-(p-p_0)^2/2\sigma_p^2}, \tag{34}$$

where the pressure variance σ_p is given by

$$\sigma_p^2 = \frac{\pi E_c^2}{2} \int_{q_l}^{q_s} dq q^3 \langle \tilde{h}^*(\mathbf{q}) \tilde{h}(\mathbf{q}) \rangle. \tag{35}$$

This prediction is tested and confirmed in Fig. 12. In these simulations, the equivalent of an elastic block composed of up to 512^3 atoms is studied. A nominal contact pressure $p_0 = 0.3$ was applied and Young's modulus, Poisson ratio, and Hurst exponent were $E=2.4342$, $\nu=1/3$, and $H=0.5$, respectively. The long wavelength cutoff is $q_l=0.04/512$, i.e., the 512th fraction of the smallest value for q_s. The calculated value of the pressure variance is $\sigma_p=0.079$.

The theoretical treatment extends to descriptions in which the shortest wavelengths are not fully resolved. When the discretization of the manifold is increased with respect to the short wavelength cutoff q_s, which was introduced in Eq. (21), the pressure histograms remain Gaussian and as predicted, they become less broad. For a comparison of theory and simulation in the case of small magnification, we integrated on the right-hand side of Eq. (35) only to an effective upper cutoff of $q_{s,\mathrm{eff}}=2\pi/a$, which replaced q_s. This is similar to but not exactly the same procedure as reducing the magnification as suggested in the theory. In the theory, the small wavelength components in the substrate are eliminated rather than those in the slider. Thus, the minor discrepancy between theory and calculation at large magnification does not stem from an error in theory. Instead, the dispersion effects within the Brillouin zones are responsible. They make the effective spring constants increase less with the magnitude of the wavelength q than in the continuum limit, which explains why the Gaussian distribution for, say $q_s a=1.24$, is (marginally) broader in the simulations than in the analytical calculations.

To summarize, the agreement between theory and simulations anticipates not only the correctness of the theory of full, nonadhesive contacts but also the feasibility of the current methodology. The computational time to accumulate the distributions displayed in Fig. 12 takes a little less than 2 hours on an Intel 875P processor.

C. Real contact without adhesion

The topographies of real surfaces do not necessarily have the properties that theoreticians consider within their models. In particular, the Fourier transforms of the height profiles $\tilde{h}(\mathbf{q})$ may be correlated in higher order. Such correlations potentially lead to deviations between theory on the one hand and experiment or numerically exact solutions on the other hand. In this section, we would like to demonstrate that our methodology can be used to not only study artificially constructed but also realistic roughness profiles. While we do not attempt to elaborate on the contact mechanics for realistic roughness profiles, we would like to assess whether the pressure distribution in realistic contacts corresponds to those predicted theoretically for nonadhesive, randomly rough surfaces. A detailed analysis of the contact mechanics based on realistic surface geometries is beyond the scope of the present paper, partially due to the lack of sufficient experimental data to make statistically significant assertions.

Height difference correlation functions $C_2(r)$ of a machined and grinded steel surface are shown in Fig. 13. Each of the three functions shown were averaged over different scans of length 20 μm. The accumulated second-order correlation functions have the same features as randomly rough surfaces, however, as alluded to above, higher-order correlation functions $C_{n>2}(\mathbf{r},\mathbf{r}',\ldots)$ may have properties that are different than those of randomly rough surfaces. Our surface of interest can be characterized by a Hurst roughness exponent $H=0.84$. The longest length scale on which roughness is found is approximately 0.3 μm, and the experimental data is not resolved below 10 nm.

In order to obtain fully converged and statistically meaningful pressure profiles, we only simulated the contact of ridges rather than the contact of the complete interfaces. For this purpose, the elastic manifold is discretized into 2^{16} units

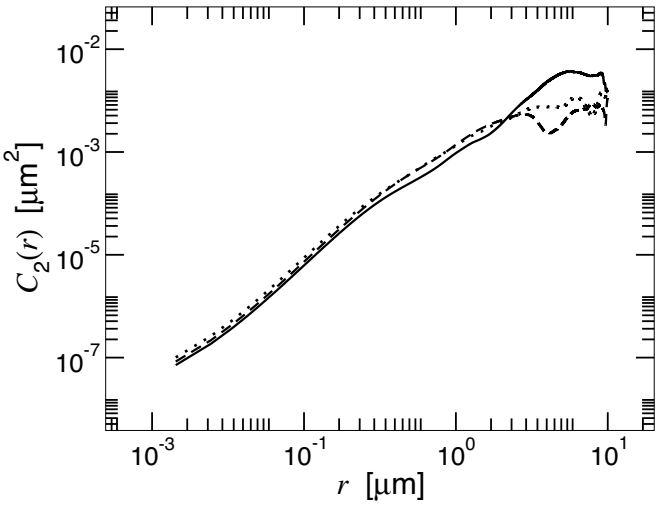

FIG. 13. Height-difference correlation function in a 2D plane for three different slices of a realistic surface. The values of the parameters in the corresponding self-affine model are $H=0.84$, $q_s=2\pi \times 10^{-3}/a$.

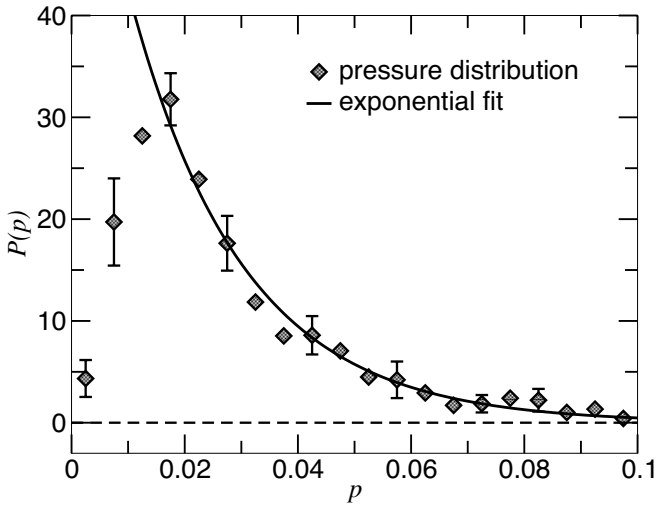

FIG. 14. Pressure distribution on the contact region between two elastic bodies with realistic interfaces. The solid line shows an exponential fit to the tail of the distribution.

each being associated with a linear length of $a \approx 3$ Å The pressure histogram was averaged over eight essentially uncorrelated profiles of the experimental data and the result is displayed in Fig. 14. The nominal, normal pressure used in these calculation was $p=10^{-3}E$, which lead a relative true contact area of approximately 4%.

Figure 14 reveals that at very small pressures, $P(p)$ vanishes linearly with decreasing p, which demonstrates that our results are converged.[38] At medium and large pressures, $P(p)$ decays exponentially with increasing p in contradiction to what one would expect for randomly rough surfaces.[8] Exponential tails were also identified by Hyun *et al.*[4] and Luan *et al.*[5] for randomly rough surfaces. However, it is not clear whether they found the exponential tails due to discretization effects as suggested by Persson[38] or due to jamming as claimed by the original authors. Settling this debate will require further investigation, which is beyond the scope of the present paper.

V. CONCLUSIONS

In this work, we have put into practice a molecular dynamics methodology, which allows one to replace a semi-infinite, harmonic solid with a single layer of atoms. Only periodic structures were considered, which made it possible to represent the (effective) elastic interactions between surface atoms in reciprocal space so that displacements associated with different wave vectors do not couple. The effective spring constants were calculated numerically by averaging the thermal fluctuations of surface atoms, i.e., their static, elastic Green's functions. These simulations were done on moderately sized crystals with eight or fewer elementary cells in each spatial dimension. The results obtained for those reference crystals can be extrapolated to arbitrarily large systems with the help of an appropriate representation. The effective elastic interactions that we obtain with our methodology agree numerically with all analytically exact solutions known to us. The advantage of our approach is that—unlike analytical solutions—computation of the elastic coupling does not become much more involved for complex interactions.

Once the effective coupling between surface atoms are determined, their knowledge can be used in Green's function molecular dynamics simulations of semi-infinite, elastic solids. The main advantages of GFMD appear to be its low computational cost, that is, each time step is relatively cheap, and its fast rate of convergence, i.e., only few time steps are required to equilibrate elastic manifold that is pressed against a rough substrate. Part of the reason for this behavior is that sound waves do not reflect in the Green's function layer, while many coarse-graining techniques suffer from low transmission of vibrations at the interface between two levels of discreteness. Moreover, when used as a solver for elastic continuum mechanical problems, it seems that the Green's function layer can be chosen much coarser than grids of conventional numerical methods such as finite elements.

The usefulness of GFMD was demonstrated by applying it to a few selected contact mechanical problems. We showed that the Hertzian contact and self-affine contacts can be modeled accurately with relatively small computational effort. We also investigated the theoretical prediction for the pressure distribution in nonadhesive contacts between an elastic, semi-infinite solid and a rigid, self-affine fractal substrate and confirmed the presence of Gaussian distributions that broaden when the level of discreteness of the description is increased. Most importantly, however, it turned out that GFMD is able to produce fully converged pressure distributions $P(p)$ for the contact between a solid and a rigid ridge, whose roughness profile was taken from experimental data. Here, fully converged refers to the situation where the pressure distribution remains (essentially) invariant when the discretization of the elastic manifold is increased. In these

calculations, we found that $P(p)$ vanishes linearly with p as p approaches zero, while $P(p)$ decreased exponentially with increasing p for intermediate and large values of p.

The above-mentioned advantages of GFMD do not come without cost. Incorporating plastic deformation is presently not feasible. Even allowing for simple anharmonicity in a numerically exact fashion will require substantial coupling of displacements associated with different wave vectors. This will slow down the simulations tremendously. Including roughness and chemical heterogeneity within GFMD will also be conceptually challenging. However, as long as roughness and heterogeneity are not too extreme, it may be possible to represent the effective elastic interactions in a hybrid fashion in real and reciprocal space without too much computational overhead.

Note added in proof. The analytical solution for the pressure profile in full contact, Eqs. (34) and (35), had originally been stated by Greenwood.[41]

ACKNOWLEDGMENTS

The authors would like to thank M. O. Robbins, B. N. J. Persson, Y. Saito, C. Denniston, and G. Bartels for useful discussions. The authors are also grateful to D. Shakhvorostov for providing us with experimental data and to NSERC and the National Science Foundation under Grant No. PHY99-0794.

*mmuser@uwo.ca; http://publish.uwo.ca/~mmuser/

[1] L. Goldstein, F. Glas, J. Y. Marzin, M. N. Charasse, and G. Le Roux, Appl. Phys. Lett. **47**, 1099 (1985).
[2] V. A. Shchukin and D. Bimberg, Rev. Mod. Phys. **71**, 1125 (1999).
[3] S. Cai and B. Bhushan, Wear **259**, 1408 (2005).
[4] S. Hyun, L. Pei, J. F. Molinari, and M. O. Robbins, Phys. Rev. E **70**, 026117 (2004).
[5] B. Luan, S. Hyun, M. O. Robbins, and N. Bernstein, Mater. Res. Soc. Symp. Proc. **841**, R7.4.1 (2005).
[6] L. Pei, S. Hyun, J. F. Molinari, and M. O. Robbins, J. Mech. Phys. Solids **53**, 2385 (2005).
[7] L. Wenning and M. H. Müser, Europhys. Lett. **54**, 693 (2001).
[8] C. Yang, U. Tartaglino, and B. N. J. Persson, Eur. Phys. J. E **19**, 47 (2006).
[9] R. E. Rudd and J. Q. Broughton, Phys. Rev. B **58**, R5893 (1998).
[10] J. Q. Broughton, F. F. Abraham, N. Bernstein, and E. Kaxiras, Phys. Rev. B **60**, 2391 (1999).
[11] S. Curtarolo and G. Ceder, Phys. Rev. Lett. **88**, 255504 (2002).
[12] W. A. Curtin and R. E. Miller, Modell. Simul. Mater. Sci. Eng. **11**, R33 (2003).
[13] V. K. Tewary, Adv. Phys. **22**, 757 (1973).
[14] S. A. Adelman and J. D. Doll, J. Chem. Phys. **61**, 4242 (1974).
[15] S. A. Adelman and J. D. Doll, J. Chem. Phys. **64**, 2375 (1976).
[16] H. Uemura, Y. Saito, and M. Uwaha, J. Phys. Soc. Jpn. **72**, 2856 (2003).
[17] Y. Saito, J. Phys. Soc. Jpn. **73**, 1816 (2004).
[18] V. K. Tewary, Phys. Rev. B **69**, 094109 (2004).
[19] R. E. Rudd and J. Q. Broughton, Phys. Rev. B **72**, 144104 (2005).
[20] R. Kubo, Rep. Prog. Phys. **29**, 255 (1966).
[21] W. Cai, M. de Koning, V. V. Bulatov, and S. Yip, Phys. Rev. Lett. **85**, 3213 (2000).
[22] G. G. Batrouni, A. Hansen, and J. Schmittbuhl, Europhys. Lett. **60**, 724 (2002).
[23] B. Fraser, C. Denniston, and M. H. Müser, J. Polym. Sci., Part B: Polym. Phys. **43**, 970 (2005).
[24] B. N. J. Persson, J. Chem. Phys. **115**, 3840 (2001).
[25] B. N. J. Persson, O. Albohr, U. Tartaglino, A. I. Voloktin, and E. Tosatti, J. Phys.: Condens. Matter **17**, R1 (2005).
[26] L. D. Landau and E. M. Lifshitz, *Statistical Physics* (Pergamon, New York, 1968).
[27] B. C. Clark, R. Herman, and R. F. Wallis, Phys. Rev. **139**, A860 (1965).
[28] K. L. Johnson, *Contact Mechanics* (Cambridge University Press, New York, 1985).
[29] B. Q. Luan and M. O. Robbins, Nature (London) **435**, 929 (2005).
[30] P. Meakin, *Fractals, Scaling and Growth far from Equilibrium* (Cambridge University Press, New York, 1997).
[31] M. H. Müser, L. Wenning, and M. O. Robbins, Phys. Rev. Lett. **86**, 1295 (2001).
[32] M. Born and K. Huang, *Dynamical Theory of Crystal Lattices* (Clarendon, Oxford, 1956).
[33] T. Schneider and E. Stoll, Phys. Rev. B **17**, 1302 (1978).
[34] P. Español and P. Warren, Europhys. Lett. **30**, 191 (1995).
[35] L. D. Landau and E. M. Lifshitz, *Theory of Elasticity* (Pergamon, Oxford, 1986).
[36] J. C. Ehrhardt, IEEE Trans. Signal Process. **41**, 1469 (1993).
[37] L. Kogut and I. Etsion, Tribol. Trans. **46**, 383 (2003).
[38] B. N. J. Persson, cond-mat/0603807 (unpublished).
[39] B. N. J. Persson, F. Bucher, and B. Chiaia, Phys. Rev. B **65**, 184106 (2002).
[40] A. W. Bush, R. D. Gibbson, and T. R. Thomas, Wear **35**, 87 (1975).
[41] J. A. Greenwood, Proc. Inst. Mech. Eng., Part J: J. Eng. Tribol. **210**, 281 (1996).